

Technological applications of organo-montmorillonites in the removal of pyrimethanil from water: adsorption/desorption and flocculation studies

Federico M. Flores^{1,2} · Tomas Undabeytia² · Esmeralda Morillo² · Rosa M. Torres Sánchez¹

Received: 6 October 2016 / Accepted: 10 April 2017 / Published online: 25 April 2017
© Springer-Verlag Berlin Heidelberg 2017

Abstract Pyrimethanil (2-aniline-4, 6-dimethylpyrimidine, PRM) is used in fruit packing plants to control fungal infections and diseases. The effluents greatly polluted with this fungicide, as a point source contamination, need to be technologically treated for their regeneration before they reach water bodies. This work evaluates the use of organo-montmorillonites, synthesized in our laboratory, for their application in adsorption and coagulation/flocculation processes for the removal of PRM from water. The adsorption-desorption performance of PRM in a raw montmorillonite (Mt) and several organo-montmorillonites (organo-Mt) obtained by different amounts and types of exchanged surfactants (octadecyltrimethylammonium (ODTMA) and didodecyltrimethylammonium (DDAB) bromides and benzyltrimethylammonium chloride (BTMA)) was studied. The PRM adsorption on raw Mt was assigned mainly to an interlayer occupancy, while hydrophobic interactions between PRM and the surfactants in the exchanged samples increased PRM adsorption, which was correlated with the surfactant loading. PRM desorption showed irreversible behavior in raw Mt, which changed to reversible for organo-Mt samples, and was also correlated with the increase of surfactant loading.

Two of the organo-Mt with high surfactant loading (twice the CEC) were assayed for the removal of commercial PRM in coagulation/flocculation tests, and their performance was compared to that of the native clay (Mt). The use of the organo-Mt produced flocculation at a very low ratio (0.5 g L^{-1}), whereas no flocculation was observed with Mt. These results proved the feasibility of the use of organo-Mt for the treatment of wastewater contaminated with PRM using a low organo-Mt/liquid ratio.

Keywords Montmorillonite · Organo-montmorillonite · Pyrimethanil · Adsorption · Desorption · Flocculation

Introduction

High amounts of different fungicides (thiabendazole, thiophanate-methyl, fludioxonil, etc.) are applied to grapes, apples, and tomatoes annually to prevent fungal infections and diseases and to maintain the agro-industries' production with good economic performance (Latorre et al. 2002; Anfossi et al. 2006). Since 2004, due to fungal resistance to thiabendazole generated by its intensive use, new effective fungicides against blue (*Botrytis cinerea*) and gray mold (*Lobesia botrana*), including pyrimethanil (PRM) have been incorporated (Sholberg et al. 2005; Komárek et al. 2010; Caiazza et al. 2014). PRM is also used in grapevines, being one of the fungicides most resistant to degradation of the anilinopyrimidine family used in this crop (Cabras and Angioni 2000). The degradation of fungicides depends on the chemical nature of the fungicide compound as well as on the chemical and physical properties of the soil (Singh and Tandon 2015). PRM is adsorbed on soil up to 80% after 24 h, with half-time degradation ($t_{1/2}$) of about 50 and 75 days in the presence and in the absence of light, respectively (Vanni et al. 2003, 2006).

Responsible editor: Angeles Blanco

Electronic supplementary material The online version of this article (doi:10.1007/s11356-017-9016-3) contains supplementary material, which is available to authorized users.

✉ Rosa M. Torres Sánchez
rosats@cetmic.unlp.edu.ar; rosa.torres@gmail.com

¹ Centro de Tecnología de Recursos Minerales y Cerámica (CETMIC, CONICET-CCT La Plata-CIC), Camino Centenario y 506, CC 49, B1897ZCA M.B. Gonnet, Provincia de Buenos Aires, Argentina

² Instituto de Recursos Naturales y Agrobiología de Sevilla (IRNAS-CSIC), Apartado, 1052 Seville, Spain

The application rates of PRM in Europe range from an average of 600 g ha^{-1} in apple orchards to 1 kg ha^{-1} in vineyards (EFSA 2006), these amounts increasing up to five times during the plant growing season (Verdisson et al. 2001). The toxicity of PRM is not dependent on the trophic level but is specific to the species (Seeland et al. 2012). A PRM formulation at a semifield scale mimicking worst-case scenarios of soil contamination was found to be highly toxic when tested against the standard soil test organisms (Gil et al. 2015).

Due to its mode of application, it may reach the ground and surface waters due to rain or spray drift. Its use on apples and pears (post-harvest treatment) in packing plants also generates serious pollution of water bodies, as a point source of contamination that needs to be solved technologically.

Montmorillonite (Mt) and organo-montmorillonite (organo-Mt) have been used as adsorbents for a variety of herbicides (Nir et al. 2000; Maqueda et al. 2013; Ren et al. 2014; Gu et al. 2015; Dutta and Singh 2015) and fungicides (Lombardi et al. 2003; Gamba et al. 2015; Flores et al. 2016). Mt can be modified to obtain organo-Mt through cation exchange and electrostatic reactions with quaternary ammonium compounds (QAC). The QAC introduced in the Mt interlayer and/or outer surfaces can act as a partitioning medium for the adsorption of nonionic organic compounds (Bartelt-Hunt et al. 2003; Patel et al. 2010; Dutta and Singh 2015), by conferring a hydrophobic character and modifying their electric charges (Bianchi et al. 2013) regarding Mt. The sorption capacity of nonionic organic compounds in organo-Mt samples has been found to be highly dependent on the molecular structure and the loading amount of the QAC used (Bartelt-Hunt et al. 2003). Particularly, Smith and Galan (1995) assigned the solute uptake to adsorption and partition mechanisms when the QAC has one or more long alkyl chain functional groups and to an adsorption mechanism when the QAC has short alkyl chain or aryl functional groups.

Increasing environmental awareness coupled with more stringent regulation standards has triggered various industries to challenge themselves in seeking appropriate wastewater treatment technologies (Teh et al. 2016). Therefore, the objective of this paper is to study the adsorption-desorption of PRM using Mt and organo-Mt samples with different contents of octadecyltrimethylammonium and didodecyltrimethylammonium bromides and benzyltrimethylammonium chloride.

The novelty of this study is the use of a commercial Mt from Castiglioni (Argentina) to prepare the sorbents. So far, in most of the studies conducted with the clay mineral, Mt reference materials were used (mostly of the Clay Minerals Society). Since the clay-organic interactions will vary according to the nature of the clay mineral (charge layer, type of interlayer cation, etc.), therefore, this type of study must be carried out with commercial products. Moreover, in fruit and wine juice clarification treatments, Mt has been widely used as a simple flocculant (Savic et al. 2014) and in water treatments, Mt is widely used for coagulation-flocculation in combination with other agents such as polymers (Rytwo et al. 2013). Likewise, the organo-Mt has shown a coagulation effect (Hojjiyev et al. 2016); while in water treatments, its use as a single flocculating agent has not been well-addressed yet.

In order to determine the mechanisms of PRM adsorption, the adsorption products were characterized by X-ray diffraction (XRD), Fourier transform infrared spectroscopy (FTIR), and zeta potential (ZP) measurements. PRM desorption studies were performed on all adsorption products to evaluate their reversibility. In addition, a flocculation study, by measuring turbidity, was conducted on some organo-Mt samples with PRM adsorbed in order to evaluate its improvement in the separation process, for the organo-Mt samples possible application in wastewater treatment from fruit packing plants.

Experimental section

Materials

Na-Mt (>99%) (Magnoli et al. 2008), labeled as Mt, was provided by Castiglioni Pes and Cia. (Lago Pellegrini deposit, Rio Negro, North Patagonia, Argentina) and used as received. The structural formula obtained from the chemical analysis was $[(\text{Si}_{3.89}\text{Al}_{0.11})(\text{Al}_{1.43}\text{Fe}^{3+}_{0.28}\text{Mg}_{0.30})\text{O}_{10}(\text{OH})_2]\text{Na}^{+}_{0.41}$ and its main properties were isoelectric point (IEP) $\text{pH} = 2.7$, specific surface area (SSA) = $34.0 \text{ m}^2 \text{ g}^{-1}$, total specific surface area (TSSA) = $621 \text{ m}^2 \text{ g}^{-1}$ (Magnoli et al. 2008), and cationic-exchange capacity (CEC) = $0.825 \text{ mmol g}^{-1}$ (Gamba et al. 2015).

PRM (Fig. 1b) PESTANAL®, analytical standard (purity 99.9%) was supplied by Fluka-Sigma-Aldrich and used as

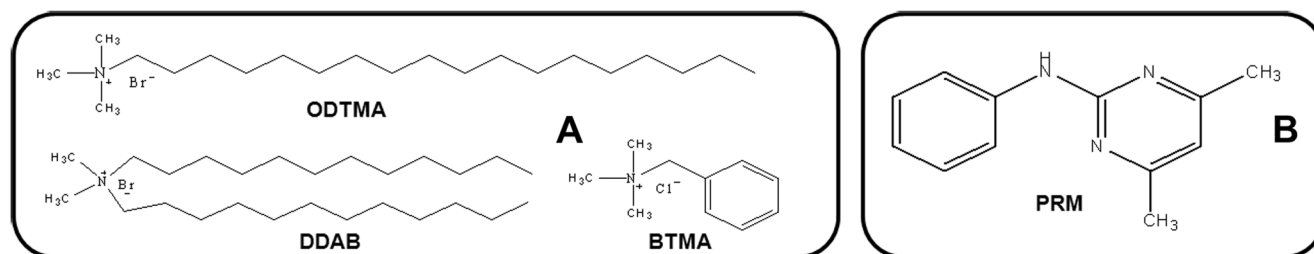


Fig. 1 Molecular structure of the different surfactants (A) employed in the organo-Mt synthesis and adsorbate studied, PRM (B)

received. Its physicochemical properties are MW = 199.25 g mol⁻¹, solubility in water = 121 mg L⁻¹ at 25 °C, and pKa = 3.52 (weak base) (PPDB 2011). For flocculation studies, a commercial PRM Pyrus 400 SC from Cheminova® was employed and denoted PRMc.

Octadecyltrimethylammonium bromide [C₁₈H₃₇N(CH₃)₃Br] (ODTMA, Fig. 1a) (≥97%), molecular weight (MW) = 392.50 g mol⁻¹ and critical micelle concentration (CMC) = 0.3 mM (Rosen 1989), and didodecyldimethylammonium bromide [(C₁₂H₂₅)₂N(CH₃)₂Br] (DDAB, Fig. 1a), (≥97%) MW = 462.63 g mol⁻¹ and CMC = 0.07 mM (Para et al. 2011), were supplied by Aldrich Chemical Co. (Milwaukee, WI). Benzyltrimethylammonium chloride [C₆H₇N(CH₃)₃Cl] (BTMA, Fig. 1a) (97%), MW = 185.69 and CMC = 3.6 mM (García-Antón and Guiñón 1991), was provided by Fluka (Buchs, Switzerland). All surfactants were used as received. In the preparation of the organo-Mt at several surfactant loadings, the corresponding concentrations of ODTMA or BTMA solutions were kept under stirring (200 rpm) for 2 h at 60 °C with 10 g L⁻¹ of Mt, while for DDAB a suspension of 5 g L⁻¹ of Mt was used instead. For ODTMA exchanged samples (OMt), the amounts corresponding to 10, 50, and 150% with respect to the Mt CEC were used. For DDAB exchanged samples (DMt), the surfactant amount used was only to attain an exchange of 150% relative to the Mt CEC in order to obtain the best hydrophobic organo-Mt (Sun et al. 2013). The QAC used for the preparation of all organo-Mt samples was over the respective CMC values. Particularly, to attain a BTMA exchanged Mt close to 100% CEC, a BTMA concentration corresponding to 500% CEC (Polubesova et al. 1997) was used. All products were washed five times with distilled water to remove the counterion excess (tested by AgNO₃), lyophilized, and ground manually in an agate mortar. The real surfactant loading for all organo-Mt samples was obtained by elemental analysis of carbon (Table 1). The products obtained were labeled as follows: XMtY, where X = O, B or D indicate the surfactants ODTMA, BTMA, or DDAB, respectively, and Y represents the real surfactant loading as a percentage of the CEC value.

Carbon analyses were performed using elemental analyzer LECO CHNS 932, and average values from three parallel measurements performed for each sample were used.

PRM adsorption-desorption

The adsorption experiments were conducted in batch conditions, with an adsorbent/adsorbate ratio of 1 g L⁻¹, using a PRM concentration range from 1 to 80 mg L⁻¹, for 24 h, at 20 °C, under continuous stirring (200 rpm) in Corex glass bottles. After the contact time, the suspensions were centrifuged at 6000 rpm for 15 min. The solids were washed five times with distilled water and freeze-dried for further characterization. The concentration of PRM in the supernatants was analyzed by high performance liquid chromatography (HPLC) coupled with UV-visible detection (λ = 270 nm) using a Shimadzu HPLC C18 column (4.6 mm × 150 mm, 4.6 μm). The mobile phase was a 70/30 acetonitrile/water mixture flowing at 0.8 mL min⁻¹. The injected volume was 20 μL. The presence of different amounts of surfactants was checked to see that it did not interfere with the PRM determination. The amount of adsorbed PRM, Q_{ADS}, (μmol PRM/g clay) was determined as the difference between the initial PRM concentration (C_i) and after contact time (C_e).

Isotherms were fitted to Langmuir model according to Eq. 1. This model indicates that adsorption occurs as a monolayer, at a finite number of defined identical and equivalent localized sites, without any interaction between the adsorbed molecules, including adjacent sites (Foo and Hameed 2010).

$$Q_{ADS} = \frac{Q_{max} \cdot K_L \cdot C_e}{1 + K_L \cdot C_e} \tag{1}$$

where Q_{ADS} is the PRM adsorbed amount, Q_{max} is the maximum adsorption capacity, C_e is the PRM concentration at equilibrium, and K_L is the Langmuir constant, related to the reaction free energy. Generally, a high Q_{max} and high K_L are appropriate for good adsorbents (Marco-Brown et al. 2014).

Isotherms were also fitted to the linear Freundlich model according to Eq. 2, which describes a nonideal process, reversible adsorption and is not limited to monolayer formation.

Table 1 Suspension pH, zeta potential, and apparent particle diameter (Dapp) for indicated samples

| Sample | Before PRM adsorption | | | After PRM adsorption | | |
|--------|-----------------------|---------------------|------------|----------------------|---------------------|------------|
| | pH | Zeta potential (mV) | Dapp (nm) | pH | Zeta potential (mV) | Dapp (nm) |
| Mt | 6.5 | -37.0 ± 1.6 | 674 ± 51 | 6.4 | -34.6 ± 0.5 | 641 ± 26 |
| BMt50 | 6.0 | -30.6 ± 1.2 | 1174 ± 72 | 5.8 | -15.9 ± 0.2 | 1778 ± 32 |
| BMt99 | 6.1 | -29.4 ± 0.6 | 2207 ± 45 | 5.5 | -31 ± 1 | 2289 ± 108 |
| OMt10 | 6.4 | -34.2 ± 1.4 | 788 ± 17 | 5.4 | -32.0 ± 0.8 | 951 ± 22 |
| OMt50 | 5.9 | -17.7 ± 0.8 | 1515 ± 53 | 5.0 | -15.8 ± 0.4 | 2134 ± 61 |
| OMt149 | 5.4 | 27.9 ± 0.3 | 3022 ± 97 | 5.6 | 28.3 ± 0.9 | 3778 ± 48 |
| DMt150 | 5.4 | 27.3 ± 0.6 | 4586 ± 106 | 5.6 | 26.6 ± 0.6 | 5634 ± 97 |

This empirical model can be applied to multilayer adsorption and in heterogeneous systems (Foo and Hameed 2010).

$$\log Q_{\text{ADS}} = \log K_F + \frac{1}{n} \cdot \log C_e \quad (2)$$

where $1/n$ is a dimensionless number and is a measure of the adsorption intensity, and K_F is a Freundlich constant.

The Sips model was also used for fitting the isotherms according to Eq. 3, which is the combination of Langmuir and Freundlich models. For low concentration is like Freundlich isotherm while for high concentration is similar to Langmuir isotherm (Foo and Hameed 2010).

$$Q_{\text{ADS}} = \frac{Q_{\text{max}} \cdot (K_s \cdot C_e)^{1/n}}{1 + (K_s \cdot C_e)^{1/n}} \quad (3)$$

where K_s is a Sips constant.

The Dubinin-Radushkevitch model (D-R) was used too for fitting the isotherms according to Eq. 4. This model is more general than the Langmuir model since it does not assume homogeneous surfaces or constant adsorption potential (Kuo et al. 2008).

$$Q_{\text{ADS}} = Q_{\text{max}} \cdot e^{-K_{\text{DR}} \cdot \varepsilon^2} \quad (4)$$

where K_{DR} is a D-R constant and is related to the mean free energy of adsorption per mole of adsorbate; ε is the Polanyi potential, which is obtained from C_e as follows:

$$\varepsilon = RT \ln \left(1 + \frac{1}{C_e} \right) \quad (5)$$

where R is the gas constant and T is the temperature (K).

From K_{DR} it is possible to calculate the mean free energy of the adsorption (E) (Eq. 6).

$$E = (2K_{\text{DR}})^{-1/2} \quad (6)$$

Desorption experiments were performed, after adsorption equilibrium was reached for the points corresponding to PRM initial concentrations of 3, 40, and 80 mg L⁻¹ by removing half of the supernatant after centrifugation (6000 rpm). Then, an equal water volume was added, under continuous stirring (200 rpm), allowing equilibration for another 24 h. This process was repeated three times and in each step the desorbed PRM was determined as indicated in the adsorption process.

Adsorption kinetics

Kinetic experiments were performed on Mt, BMt99, OMt149, and DMt150 samples. The following procedure was used: 20 mg of adsorbent was placed in Corex glass centrifuge tubes, and 20 mL of 50 mg L⁻¹ PRM solution was added to all samples, except for Mt where the PRM solution was

30 mg L⁻¹. The suspensions were maintained under continuous stirring (200 rpm) and aliquot samples were taken at 1, 10, 30, 60, 120, 360, 1080, and 1440 min and analyzed by HPLC-UV in the same way as for adsorption.

Three mathematical models were employed for the kinetic analysis: the pseudo-first order (PFO), pseudo-second order (PSO), and intraparticle diffusion (IDM) models (Bulut et al. 2008; Crini et al. 2007; Areco and dos Santos 2010; Marco-Brown et al. 2014). Equations 7, 8, and 9 describe the PFO, PSO, and IDM models, respectively:

$$\ln (q_e - q_t) = \ln q_e - k_1 t \quad (7)$$

$$\frac{t}{q_t} = \frac{1}{k_2 q_e^2} + \frac{t}{q_e} \quad (8)$$

$$q_t = k_{\text{id}} \sqrt{t} + C \quad (9)$$

where t is the time, q_e and q_t are the amounts of PRM adsorbed in equilibrium and at time t , respectively, k_1 , k_2 , and k_{id} are the rate constants for the PFO, PSO, and IDM models, respectively, and C is a constant.

Characterization methods

The PRM adsorbed samples used for characterization were those with the maximal PRM adsorption attained for each adsorbent.

XRD patterns were recorded on oriented samples, in the range $2^\circ < 2\theta < 30^\circ$, with a counting time of 10 s/step, 0.02° (2θ) step size, 40 kV, and 30 mA with CuK_α radiation using a Philips PW 1710 diffractometer.

The ZP determination was performed in Brookhaven 90Plus/Bi-MAS equipment on water suspensions (1 g L⁻¹) and also on supernatant samples coming from flocculation studies.

Apparent particle diameter determinations were achieved using the same Brookhaven equipment utilized for ZP measurements, employing the multiangle particle sizing function and dynamic light scattering (DLS). For each determination, samples were dispersed in water. The equipment operated at $\lambda = 635$ nm, 15-mW solid-state laser, scattering angle = 90° , and temperature = 25°C . The determination reproduced the apparent particle diameter of equivalent sphere, D_{app} .

FTIR was performed for all powder samples in KBr disk (1 mg of sample and 100 mg KBr). The FTIR spectra were recorded in the wavenumber range from 400 to 4000 cm⁻¹ using JASCO 6300 equipment.

Flocculation studies

Flocculation studies were performed by determining the turbidity of supernatants. For the flocculation experiments, a PRMc concentration of 250 mg L⁻¹ was used, and the solid/

liquid ratio was varied (0.1, 0.5, 1, 2, 4, and 5 g L⁻¹). The products obtained were labeled as Mt/PRMc and organo-Mt/PRMc. Suspensions for turbidity measurements were obtained with a procedure similar to that indicated by Ghimici and Nichifor (2012) for the flocculation of an amphiphilic polyelectrolyte in a clay suspension: the corresponding amount of organo-Mt (powder) was added to a suspension of PRMc stirring for 5 min at 800 rpm and then at 400 rpm for 15 min. Finally, suspensions were allowed to stand for 5 min. The supernatants were immediately analyzed employing Turbiquant 1500IR equipment. The turbidity values were expressed as percentage relative to the turbidity value (100%) of the PRMc suspension alone.

Results and discussion

Characterization of Mt and organo-Mt

XRD analysis

XRD patterns showed the d001 value shifts due to the surfactant entrance to the Mt interlayer (Fig. 2). In the case of Mt, the basal spacing of the clay increased from 1.25 to 1.39 nm. By taking into account that the clay platelet is 0.96 nm, the increase in the basal space (0.43 nm) is of the approximate width of a planar aromatic ring of BTMA (0.46 nm) (Polubesova et al. 1997). This indicated sorption of PRM molecules on a planar conformation on the clay surface. For OMt samples, the interlayer space increased with surfactant loading, in agreement with Xi et al. (2004), leading to lateral-monolayer (1.43 nm), lateral-bilayer (1.77 nm), and pseudo-trilayer

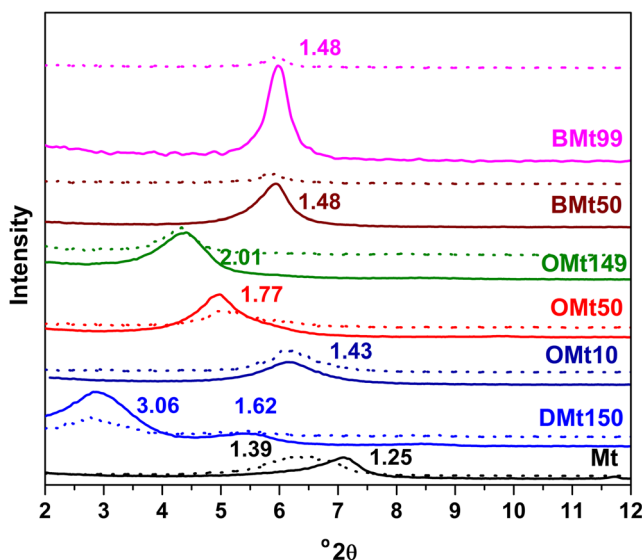


Fig. 2 XRD patterns for Mt and indicated organo-Mt samples (solid line) and these samples with adsorbed PRM (dotted line). Basal space values are expressed in nm

(2.01 nm) arrangements, for OMt10, OMt50, and OMt149 samples, respectively. For BMt samples, no changes in the basal space among them were found irrespective of the BTMA loading amount, and the increase of 0.23 nm with respect to Mt sample was assigned to the interlayer entrance of a BTMA monolayer (Polubesova et al. 1997). Among the surfactants exchanged in the Mt interlayer, DDAB (DMt150 sample) showed the largest increase (3.06 nm, Fig. 2) in agreement with data reported by He et al. (2010) and reflecting a paraffin bilayer arrangement with the appearance of the d 002 and d 003 order at 1.62 and 1.04 nm (Sun et al. 2013), respectively (Fig. S1, Supplementary material).

ZP and apparent particle diameter measurements

The Mt sample exhibited the traditional negative electric surface charge value (−37 mV) (Maqueda et al. 2013), while the OMt samples showed the classical decrease of negative electric surface charge value with a surfactant loading increase up to Mt CEC and electric charge reversal to positive when loadings were over the Mt CEC (Table 1), as shown for OMt149 and DMt150 samples (Bianchi et al. 2013). Particularly, for BMt samples a similar ZP value was found among them, without attaining the positive electric charge assigned to the BTMA surfactant loading below the CEC value (Table 1). The increase in apparent particle diameter (Dapp) with surfactant loading was assigned to the formation of large aggregates, in agreement with that found previously (Bianchi et al. 2013; Gamba et al. 2015).

A slight decrease in the suspension pH (around 1 unit of pH) was found in OMt samples with the increase in surfactant loading, which could be assigned to the electrostatic attraction of water OH⁻ and release of H⁺ due to their surface electric charge change from negative to positive. The pH of DMt150 sample followed a similar behavior to that of OMt149 sample. For BMt samples, the low neutralization of the raw Mt negative surface charges was also evidenced by a lower pH decrease with respect to Mt sample and to those attained by OMt samples.

FTIR spectroscopy

The FTIR analysis for Mt sample (Fig. S2 in Supplementary material) showed the typical bands corresponding to its structural groups: νOH, νSiO, δAlAlOH, δAlOSi, and δSiOSi at 3632, 1040, 916, 521, and 461 cm⁻¹, respectively, in agreement with data found by Gamba et al. (2015). Besides these bands, those corresponding to CH stretching vibration of the surfactants in OMt and DMt samples were observed (Fig. 3a) at around 2920 and 2850 cm⁻¹, corresponding to the asymmetric and symmetric stretching of CH₂ groups, respectively. The intensity of the bands increased and shifted to lower wavenumber values (from 2929 to 2920 cm⁻¹, and from

2856 to 2850 cm^{-1}) with ODTMA loading due to the formation of the more ordered structure of the alkyl chains (Gamba et al. 2015). These bands were not observed for BMt sample (Fig. 3a).

The appearance of the bands corresponding to bending vibration of the alkyl groups ($\delta_{\text{as}}\text{CH}_3\text{N}$ and $\delta_{\text{as}}\text{CH}_2$ at 1485 and 1468 cm^{-1} , respectively) confirmed the presence of ODTMA and DDAB surfactants in the exchanged samples (Fig. 3b). The band at 1644 cm^{-1} corresponds to water molecule deformation in all samples, with the respective decrease in intensity with ODTMA loading and the corresponding exchange of hydrated interlayer cations (Tong et al. 2010).

The infrared spectra of BTMA (Fig. 3c) showed the bands corresponding to the stretching vibrations of the phenyl group at 1492, 1480, and 1461 cm^{-1} , which shifted to lower wavenumber values when BTMA was exchanged in Mt sample (Majdan et al. 2009). This behavior, as indicated by Majdan et al. (2009), is probably due to the interaction of the π electrons of the phenyl ring with the π electrons of the oxygen of the Mt layers. The band at 1644 cm^{-1} , originated by water molecule deformation in BMt samples, had a similar behavior to that found for OMt samples, as indicated previously. The band at 1414 cm^{-1} , assigned to the α -methylene scissoring mode for the BTMA surfactant, remained on BMt samples, while that at 1389 cm^{-1} , corresponding to the bending vibration of CH_3 of the ammonium head group (Wong et al. 1997) in BTMA spectra, shifted to 1378 cm^{-1} in BMt samples assigned to strong electrostatic interactions between the N of the ammonium with Mt surface sites (Majdan et al. 2009).

PRM adsorption-desorption

The PRM adsorption-desorption isotherms are presented in Fig. 4. The PRM adsorption capacity followed the order: DMt150 sample ($\approx 330 \mu\text{mol PRM/g clay}$) > OMt149 sample ($\approx 240 \mu\text{mol PRM/g clay}$) > Mt ($\approx 156 \mu\text{mol PRM/g clay}$) > OMt50 ($\approx 113 \mu\text{mol PRM/g clay}$) > BMt50 ($\approx 105 \mu\text{mol PRM/g clay}$) > OMt10 ($\approx 94 \mu\text{mol PRM/g clay}$) > BMt99 ($\approx 80 \mu\text{mol PRM/g clay}$). Particularly, the

PRM adsorption values of Mt sample agree with that found by Baglieri et al. (2009), at low PRM concentrations, and were assigned to PRM entrance to the interlayer (Fig. 2).

The increase in the adsorption capacity of each surfactant was correlated with the loading amount and type of surfactant, which might point out the presence of a hydrophobic-type interaction between the fungicide and the surfactant (Smith and Galan 1995; Cruz-Guzmán et al. 2005; Mo et al. 2015). For OMt samples, the PRM adsorption capacity increased with the surfactant loading, contrary to that found for BMt samples. This opposite behavior between both surfactants (ODTMA and BTMA), within the PRM concentration range studied, indicated a decrease in the number of adsorption sites with the increase of BTMA loading in BMt samples, indicating a slight tendency of the PRM to adsorb on BTMA surfactant. Nevertheless, a close Q_{max} was found for both BMt samples (Table 2), which could indicate a decrease in the number of the surface sites shielded by the surfactant when the PRM concentration increased.

Particularly, the higher adsorption capacity observed in DMt150 sample could be assigned to the presence of two hydrocarbon chains in DDAB, which produce a greater hydrophobicity, originated by different conformational states of DDAB in the interlayer space (Sagitova et al. 2009) than those of OMt149 sample.

Although for two samples (OMt10 and BMt50 samples) the Langmuir (R^2) correlation coefficients were lower than those obtained with adjustment of the experimental data with the Freundlich equation (Table 2), the theoretical Q_{max} capacities attained by Langmuir equation were in line with the maximum PRM adsorption, within the C_i range evaluated (Fig. 4), for all adsorbents.

A comparison of the PRM adsorption based on K_F parameter (Table 2)—which represents the affinity of the sorbent material for the adsorbate—between Mt and organo-Mt samples with low surfactant loading cannot be made because of the different $1/n$ values attained, except for DMt150 sample (Maqueda et al. 2013). The higher affinity of PRM found ($K_F = 6.9$) for DMt150 than for Mt samples, with similar $1/n$

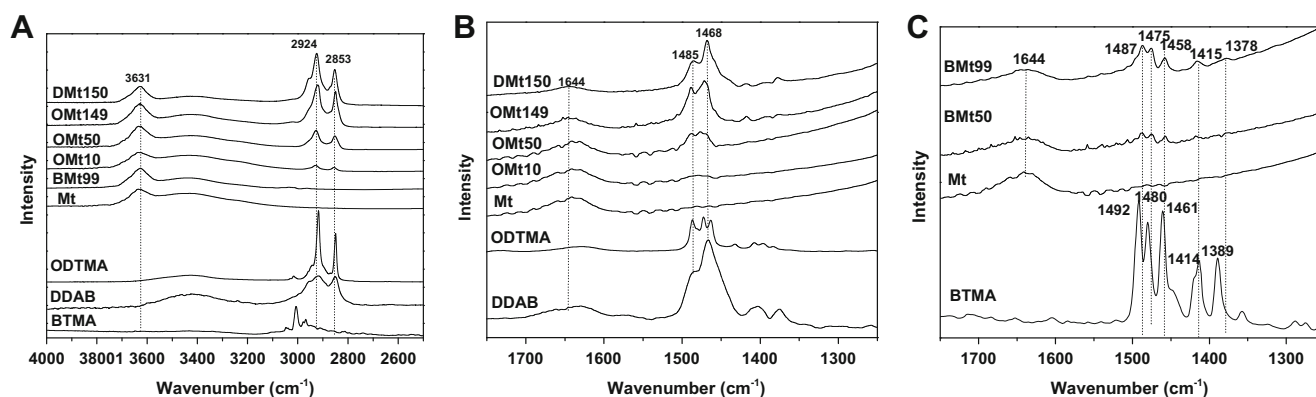


Fig. 3 FTIR spectra of neat surfactants, Mt, and organo-Mt samples

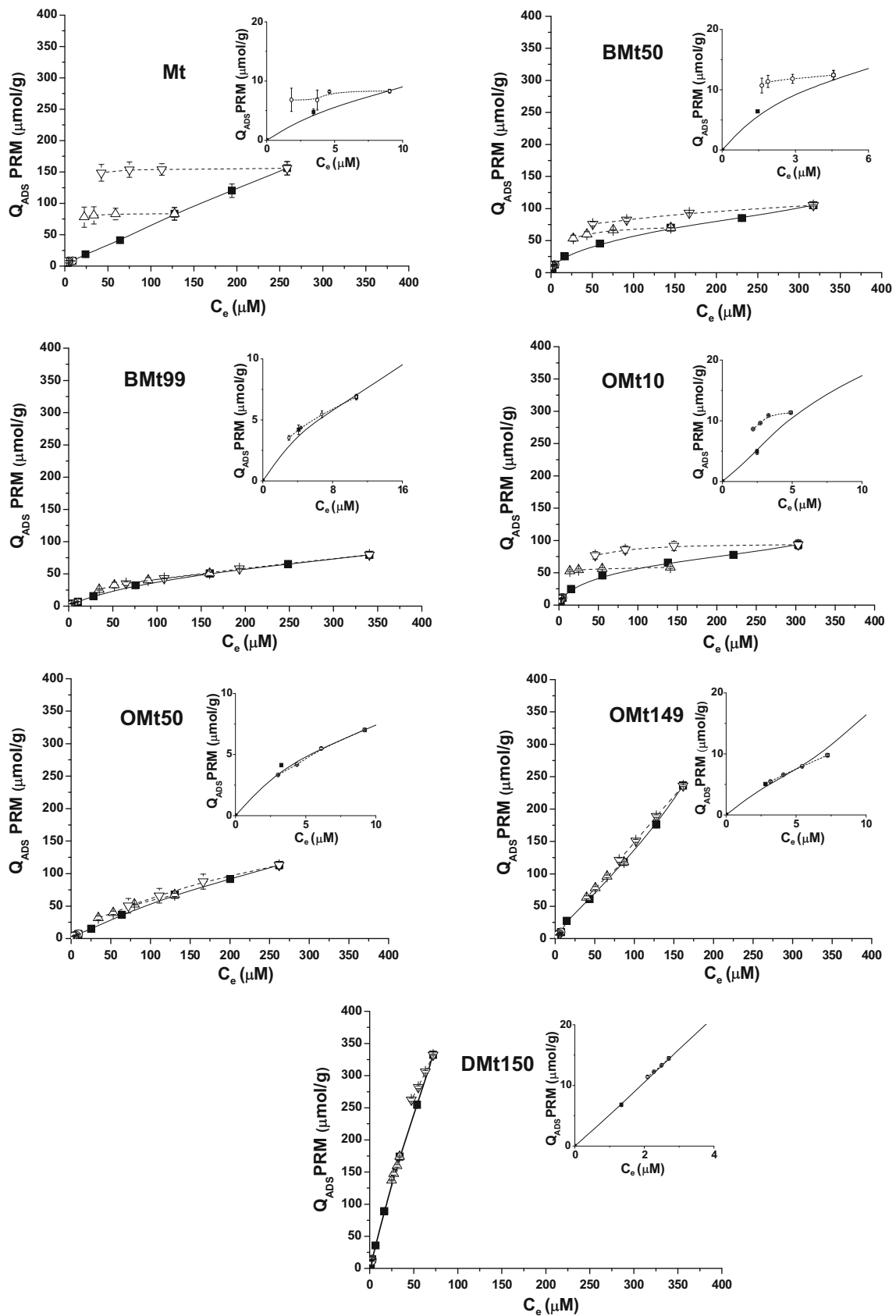


Fig. 4 PRM adsorption-desorption isotherms on the indicated samples. The inset graphs correspond to desorption of the adsorption point with 3 mg L^{-1}

Table 2 Langmuir and Freundlich parameters for PRM adsorption on Mt and organo-Mt samples

| Sample | Langmuir | | | Freundlich | | |
|---------|---------------------------------------|--|--------|-----------------------------|-------------|--------|
| | Q_{\max} ($\mu\text{mol g}^{-1}$) | K_L ($\text{L } \mu\text{mol}^{-1}$) | R^2 | K_F (L g^{-1}) | $1/n$ | R^2 |
| Mt | 1146 ± 324 | 0.0006 ± 0.0002 | 0.9999 | 0.98 ± 0.09 | 0.91 ± 0.02 | 0.9994 |
| BMt50 | 132 ± 17 | 0.009 ± 0.003 | 0.9673 | 6.0 ± 0.5 | 0.49 ± 0.01 | 0.9982 |
| BMt99 | 133 ± 10 | 0.0041 ± 0.0006 | 0.9955 | 2.0 ± 0.2 | 0.64 ± 0.02 | 0.9983 |
| OMt10 | 107 ± 13 | 0.013 ± 0.005 | 0.9525 | 6 ± 1 | 0.48 ± 0.04 | 0.9879 |
| OMt50 | 345 ± 30 | 0.0018 ± 0.0002 | 0.9991 | 1.3 ± 0.1 | 0.81 ± 0.02 | 0.9989 |
| OMt149* | – | – | – | 1.2 ± 0.2 | 1.03 ± 0.04 | 0.9972 |
| DMt150 | 1984 ± 226 | 0.0028 ± 0.0004 | 0.9997 | 6.9 ± 0.4 | 0.91 ± 0.01 | 0.9995 |

*Not fit to Langmuir

values, would support the hydrophobic interactions (DDAB/PRM) indicated previously.

The experimental points were also fitted to Sips and D-R models according to Eqs. 3 and 4, respectively. The parameters obtained are listed in Table 3.

Mt, BMt50, OMt10, and OMt149 samples did not fit Sips model; however, other samples fitted this model very well ($R^2 > 0.999$), despite their high standard deviation ($\approx 50\%$) of K_s values. The Q_{\max} obtained from Sips model was slightly higher than that found by Langmuir fit.

The D-R model fit very well all studied samples ($R^2 > 0.99$). The Q_{\max} values obtained with this model were higher than that determined with the Langmuir and Sips models. The determination of the E values could be indicative of different adsorption processes, where values ranging from 1 to 8 kJ mol^{-1} indicate physisorption processes, whereas those between 8 and 16 kJ mol^{-1} show ionic-exchange or electrostatic interactions (Kilisliloglu and Bilgin 2003; Ünlü and Ersoz 2006; Özcan et al. 2005; Hu et al. 2011; Guégan et al. 2015). The E values for OMt50, OMt149, and DMt150 samples indicated a physisorption process, supporting the assumption of the presence of hydrophobic interactions or van der Waals forces (Özcan et al. 2005), in agreement with the desorption studies that will be discussed later. Surprisingly, the E value obtained for Mt sample was also within the same value

range, in disagreement with the PRM desorption studies discussed in further paragraphs, where PRM seems to be strongly bound to Mt surface. In order to evaluate the goodness-of-fit of the E parameter determined by the D-R model, the average relative deviation (ARD) was calculated for all samples (Table S1 in Supplementary material) (Stofela et al. 2015). The high ARD values obtained for Mt and OMt149 samples (21 and 24, respectively) would explain the low E values obtained for both samples.

To describe the PRM desorption, a coefficient of hysteresis (H) was calculated (Morillo et al. 2004; Undabeytia et al. 2012) according to Eq. 10:

$$H = \frac{1/n_a}{1/n_d} \quad (10)$$

where $1/n_a$ and $1/n_d$ were obtained from adsorption and desorption curves, respectively, and by applying Eq. 2. Table 4 shows the values of H obtained for each sample and the desorption percentage for three initial PRM concentrations.

PRM desorption showed different behaviors depending on the adsorbent used. The high values of H obtained for Mt sample (Table 4) pointed out an irreversible PRM adsorption, as can be observed in Fig. 4. Contrarily, an almost reversible adsorption process was found in organo-Mt samples ($H \approx 1$),

Table 3 Sips and D-R parameters for PRM adsorption on Mt and organo-Mt samples

| Sample | Sips | | | | D-R | | | |
|---------|---------------------------------------|--|-------------|--------|---------------------------------------|---|------------------------------|--------|
| | Q_{\max} ($\mu\text{mol g}^{-1}$) | K_s ($\text{L } \mu\text{mol}^{-1}$) | $1/n$ | R^2 | Q_{\max} ($\mu\text{mol g}^{-1}$) | K_{DR} ($\text{mol}^2 \text{J}^{-2}$) | E (kJ mol^{-1}) | R^2 |
| Mt* | – | – | – | – | 2280 ± 650 | $(8.3 \pm 0.3) \times 10^{-9}$ | 7.78 | 0.9979 |
| BMt50* | – | – | – | – | 544 ± 55 | $(4.2 \pm 0.2) \times 10^{-9}$ | 10.88 | 0.9945 |
| BMt99 | 270 ± 67 | 0.0009 ± 0.0005 | 0.76 ± 0.04 | 0.9994 | 734 ± 30 | $(5.70 \pm 0.09) \times 10^{-9}$ | 9.37 | 0.9995 |
| OMt10* | – | – | – | – | 446 ± 41 | $(3.9 \pm 0.2) \times 10^{-9}$ | 11.28 | 0.9946 |
| OMt50 | 502 ± 189 | 0.00010 ± 0.00005 | 0.92 ± 0.06 | 0.9994 | 2280 ± 170 | $(7.2 \pm 0.2) \times 10^{-9}$ | 8.33 | 0.9991 |
| OMt149* | – | – | – | – | 14,940 ± 4320 | $(8.9 \pm 0.6) \times 10^{-9}$ | 7.48 | 0.9937 |
| DMt150 | 2262 ± 929 | 0.002 ± 0.001 | 0.99 ± 0.04 | 0.9997 | 17,730 ± 946 | $(7.13 \pm 0.09) \times 10^{-9}$ | 8.37 | 0.9997 |

*Not fit to Sips

Table 4 PRM desorbed percent (% *D*) and coefficient of hysteresis (*H*) of the indicated samples when treated at the initial concentration of PRM (3, 40, and 80 mg L⁻¹)

| Sample | % <i>D</i> | | | <i>H</i> | | |
|--------|-------------------------|--------------------------|--------------------------|-------------------------|--------------------------|--------------------------|
| | 3 (mg L ⁻¹) | 40 (mg L ⁻¹) | 80 (mg L ⁻¹) | 3 (mg L ⁻¹) | 40 (mg L ⁻¹) | 80 (mg L ⁻¹) |
| Mt | 13 ± 4 | 17 ± 3 | 20 ± 2 | 6.1 ± 0.4 | 14 ± 3 | 15 ± 2 |
| BMt50 | 14 ± 4 | 24 ± 3 | 28 ± 2 | 3.8 ± 1.0 | 3.1 ± 0.5 | 2.8 ± 0.3 |
| BMt99 | 49 ± 2 | 49 ± 2 | 56 ± 2 | 1.3 ± 0.1 | 1.6 ± 0.2 | 1.4 ± 0.2 |
| OMt10 | 23.7 ± 0.9 | 3 ± 2 | 22 ± 3 | 1.7 ± 0.5 | 13 ± 1 | 6 ± 2 |
| OMt50 | 52.4 ± 0.7 | 53 ± 2 | 70 ± 3 | 1.1 ± 0.1 | 1.4 ± 0.1 | 1.2 ± 0.1 |
| OMt149 | 44 ± 1 | 46 ± 2 | 49 ± 1 | 1.4 ± 0.1 | 1.2 ± 0.1 | 1.0 ± 0.1 |
| DMt150 | 21 ± 1 | 21 ± 1 | 21 ± 1 | 1.0 ± 0.1 | 1.3 ± 0.1 | 1.7 ± 0.2 |

except for BMt50 and OMt10 samples. The reversible process found in organo-Mt, with respect to that for Mt sample, could indicate weaker hydrophobic interactions of PRM with the organic phase than those that occurred with the inorganic surface of Mt. This behavior was also observed by the slight deviation of desorption with respect to the adsorption isotherms of these samples (Fig. 4).

The *H* values found were higher for Mt sample than for organo-Mt samples (Table 4), indicating a stronger interaction of the Mt surface than that of the organic coverage of organo-Mt samples. This would also explain the fact that for BMt50 and OMt10 samples, the *H* values were greater than in other organo-Mt samples. This behavior could be assigned to a partial PRM adsorption onto the Mt surface that is not fully covered by the surfactant and produces a more difficult PRM desorption. The higher *H* value found for OMt10 sample was assigned to a partial interlayer surface coverage by the surfactant and consequently, more Mt free surface was available to interact with PRM. For OMt50 sample, although the amount of surfactant loading was only 50%, the Mt interlayer surface was completely covered by the monolayer surfactant arrangement, which allowed it to form a bilayer, as observed by XRD (Fig. 2).

Kinetic adsorption

The chemical adsorption kinetics of PRM on some adsorbents may provide evidence about the adsorption mechanism that occurs in the systems studied. Table 5 shows the parameters

obtained and the correlation factor (*R*²) for all the kinetic models evaluated.

The parameters *q_e* and *k₁* for the PFO model were calculated from the intercept and slope, respectively, of the plot of ln (*q_e* - *q_t*) versus *t* (figure not shown). The low *R*² values obtained indicate that the PFO model does not fit the experimental data. This is due to two main disadvantages presented by this model: (1) linear Eq. 7 does not give a *q_e^{calc}* close to the *q_e^{exp}* value, and (2) the plot of ln (*q_e* - *q_t*) versus *t* is linear at short contact times (approximately 30 min) (Bulut et al. 2008).

Since the PFO model could not be used for understanding the adsorption kinetics of PRM on the adsorbents evaluated, the PSO model was tested. In this model, the rate at which adsorption sites are covered is proportional to the square of the number of unoccupied sites, and the number of occupied sites is proportional to the PRM adsorbed (Eq. 8). For the PSO model, the plot of *t/q_t* versus *t* (Fig. S3 in Supplementary material), was used to obtain the parameters *q_e* and *k₂* (Table 5) whose high *R*² (>0.9998) values indicated that the adsorption process is governed by PSO kinetics. Moreover, the values of *q_e* calculated from the PSO kinetics were similar to the experimental values, contrary to what happened with those calculated from the PFO model (Table 5).

Besides, in order to see whether the adsorption is governed by a diffusion process, IDM was incorporated in the kinetic analysis. From this model, when the plot *q_e* versus *t*^{1/2} results in a straight line passing through the origin, it indicates a rate-limiting step by diffusion (internal surface and pore diffusion). When the plot does not pass through the origin, it indicates

Table 5 Kinetic parameters of PRM adsorption on indicated samples

| Sample | <i>q_e^{exp}</i> (μmol g ⁻¹) | PFO | | | PSO | | | IDM | |
|--------|--|---|---|-----------------------|--|---|-----------------------|---|-----------------------|
| | | <i>k₁</i> (min ⁻¹) | <i>q_e^{calc}</i> (μmol g ⁻¹) | <i>R</i> ² | <i>k₂</i> (g μmol ⁻¹ min ⁻¹) | <i>q_e^{calc}</i> (μmol g ⁻¹) | <i>R</i> ² | <i>k_{id}</i> (μmol g ⁻¹ min ^{-1/2}) | <i>R</i> ² |
| Mt | 62.5 | 0.0034 | 9.9 | 0.8100 | 0.002 | 62.5 | 0.9999 | 0.560 | 0.4063 |
| BMt99 | 39.5 | 0.0004 | 3.1 | <0.1 | 0.019 | 38.0 | 0.9998 | 0.172 | 0.2468 |
| OMt149 | 130.0 | 0.0014 | 6.4 | 0.2902 | 0.005 | 128.8 | 0.9999 | 0.543 | 0.3135 |
| DMt150 | 195.0 | 0.0026 | 18.9 | 0.4339 | 0.002 | 194.3 | 0.9999 | 1.539 | 0.3573 |

that other processes may occur. The plot q_e versus $t^{1/2}$ (Fig. S4 in Supplementary material) showed a multilinear behavior for all samples, which indicated that the intraparticle diffusion process was involved in the adsorption process, but it was not the only one that occurred.

Characterization of PRM adsorbed samples

XRD analysis

The PRM adsorption on Mt produced a noticeable shift (0.14 nm) of basal space with respect to the raw Mt sample (Fig. 2, dotted line), pointing out the PRM entrance to the interlayer space.

The adsorption of PRM on organo-Mt samples (Fig. 2, dotted line) did not modify the basal space of the respective starting samples (Fig. 2, solid line), indicating that the subsequent PRM entrance may be shielded by the surfactant occupation of the interlayer.

ZP and apparent particle diameter measurements

The ZP values for Mt and organo-Mt samples with PRM adsorbed showed different behaviors on the outer surface of the adsorbents (Table 1).

For Mt sample, the negative electric surface charge was slightly neutralized after PRM adsorption (ZP values changed from -37.0 to -34.6 mV, Table 1).

For organo-Mt samples, the amount of PRM adsorbed generated two different situations related to the surfactant loading (Table 1). At low surfactant loading, for OMt10, OMt50, and BMt50 samples, some external or edge negative surface sites were partly screened or neutralized by PRM adsorption, decreasing the final electric negative surface charges. Particularly, for OMt10 and OMt50 samples, after PRM adsorption the pH decreased 1 pH unit, which could indicate some degree of PRM interaction with the AlO^- or SiO^- groups of the Mt edge (IEP_{pH} = 4–5.3; Pecini and Avena 2013) not yet totally neutralized by the respective surfactant. Besides, in the inner or interlayer surface, some interactions of PRM with the inorganic surface in gaps created by the arrangement of organic molecules, which explained the significant irreversibility in the PRM adsorption of OMt10 and BMt50 samples (Table 4), could also develop.

For samples with surfactant loading over or close to the CEC (DMt150, OMt149, BMt99 samples), the PRM adsorption did not change the initial electric surface charge, reflecting the prevalence of hydrophobic interactions, as also evidenced by the almost constancy of pH with PRM adsorption, except for BMt99 sample. This may be explained by the entrance of neutral PRM to the interlayer space since at the equilibrium pH values, PRM is found as a neutral species (Fig. 1b). A similar feature was

also previously reported by Gamba et al. (2017) through molecular modeling for thiabendazole adsorption in OMt samples.

An overall increase of Dapp values was found for organo-Mt samples with PRM adsorbed, with respect to the corresponding samples without PRM (Table 1). The formation of larger aggregates with PRM adsorption in OMt and DMt samples than in BMt samples could be assigned to hydrophobic interactions between particles through the PRM adsorbed on the external surface of former samples. However, in BMt samples two different behaviors could be responsible for the lower increase of Dapp values with PRM adsorption: the PRM had not adsorbed on the organic molecule and/or BTMA was mainly exchanged at the interlayer, as indicated by the almost constant ZP value (Table 1), and a low BTMA amount could interact with PRM at the external surface to form larger aggregates.

FTIR analysis

Figure 5 shows the FTIR partial spectra of PRM and Mt, OMt149, DMt150, and BMt99 samples with and without adsorbed PRM.

The band at 1615 cm^{-1} corresponds to N-H deformation in the N-phenyl-pyrimidinamine group, and according to Araña et al. (2008), after the interaction with Mt or organo-Mt complexes, this band disappears and a new band can be observed at about 1601 cm^{-1} indicating that the secondary amine group of PRM is involved in the interaction, probably through H-bonding with the surface of these complexes.

Bands at 1588 and 1567 cm^{-1} in pure PRM are assigned to $\nu\text{C}=\text{C}$ of the pyrimidine ring of PRM (Akyuz and Akyuz 2003). These bands of the aromatic pyrimidine ring are very sensitive to the type of adsorbing site. In Mt-PRM complex, these bands do not appear, but a new band is observed at 1579 cm^{-1} , which could indicate the formation of H-bondings through one of the pyrimidine-ring nitrogens. On the contrary, in DMt150-PRM and OMt149-PRM complexes, these two bands remain practically constant (at 1587 and 1563 cm^{-1}). It is important to remark that in the OMt samples, the increase of ODTMA loading produced a change from one band at 1576 cm^{-1} for OMt10-PRM samples, which shifted to 1563 cm^{-1} for OMt50-PRM sample (figure not shown), to the two bands indicated previously for OMt149-PRM and assigned to the increase in PRM adsorption (Fig. 4).

The band at 1551 cm^{-1} in PRM is assigned to N-H deformation of the aniline ring in a secondary amine. This band shifted to 1538 cm^{-1} in the DMt150-PRM and OMt149-PRM complexes (Fig. 5), corroborating the H-bonding through this NH group.

The band at 1496 cm^{-1} corresponds to $\nu\text{C}=\text{C}$ of the aniline ring of PRM and undergoes only a slight shift after interaction of the fungicide with Mt or DMt150 complex (1502 and 1498 cm^{-1} , respectively).

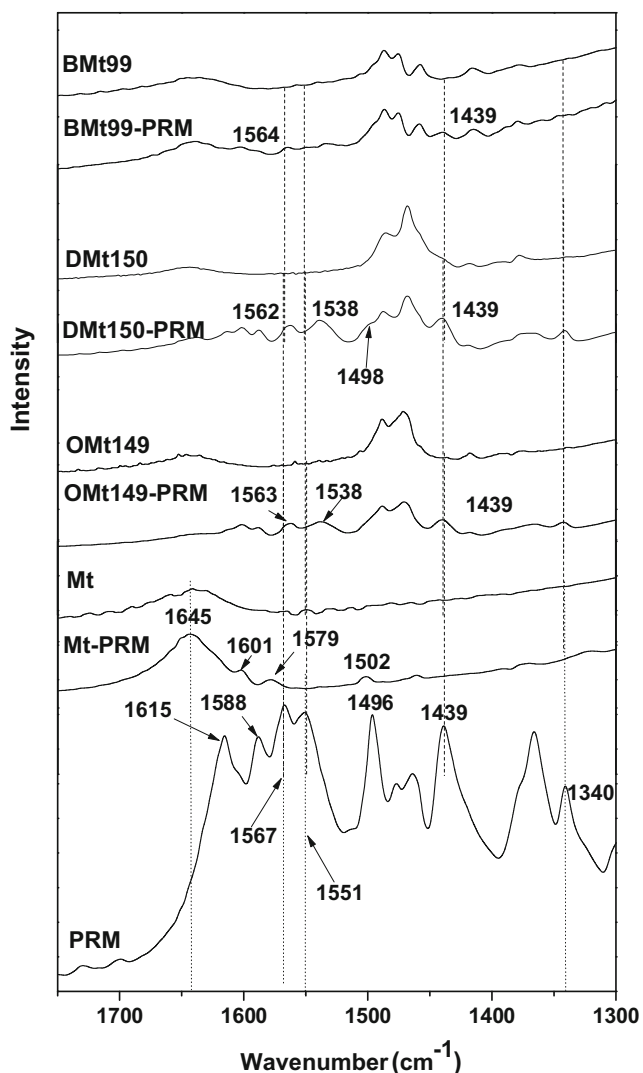


Fig. 5 FTIR spectra of indicated samples

The band at 1439 cm^{-1} in PRM spectra can be assigned to C-N stretching of the secondary amine from the pyrimidine ring. After interaction with organo-Mt complexes, it does not change; but in Mt-PRM, it does not appear.

The band at 1340 cm^{-1} in PRM spectra can be assigned to C-N stretching of arylamines from the aniline ring. In DMt150-PRM and OMt149-PRM complexes, it does not change (1340 cm^{-1}); but in Mt-PRM complex, it does not appear.

Flocculation studies

To assess the potential technological application of Mt and the organo-Mt that showed greater sorption capacity (DMt150, OMt149) in batch adsorption systems for wastewater treatment, flocculation studies of PRM_C were performed and evaluated by turbidity measurements. The influence of the solid/liquid ratio with DMt150, OMt149, and Mt samples on PRM_C adsorption was also analyzed by maintaining the PRM_C initial concentration at 250 mg L^{-1} (Fig. 6). The maximum adsorption per gram of

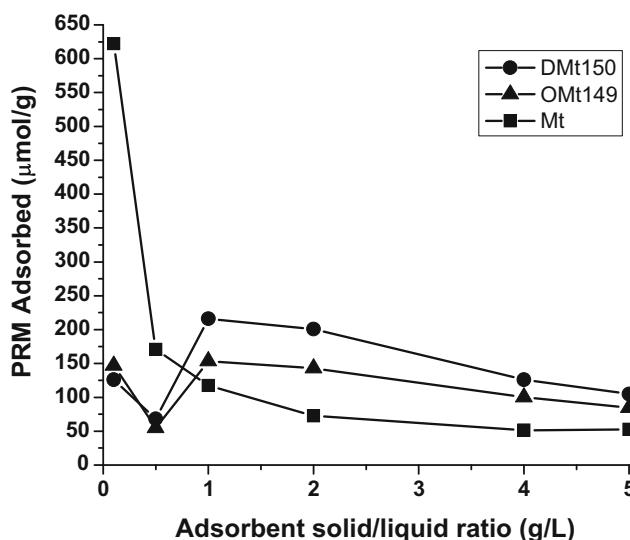


Fig. 6 Adsorbed amount of PRM_C versus adsorbed concentration of indicated samples

adsorbent was found at a concentration of 1 g L^{-1} and 0.1 g L^{-1} for both organo-Mt and Mt, respectively.

A decrease in relative turbidity of DMt150/PRM_C and OMt149/PRM_C samples was found for solid/liquid ratios of 0.5 and 1 g L^{-1} , respectively (Fig. 7), indicating a large and rapid flocculation. Turbidity increased at larger ratios due to increased repulsion between the positively charged organoclay particles. The lower amounts of floccules observed at a ratio above 1 g L^{-1} (Fig. 7) explained the lower sorbed amounts at higher ratios due to higher PRM concentrations in the suspensions (Fig. 6). Contrarily, Mt/PRM_C sample showed higher turbidity than the initial PRM_C suspension for all solid/liquid ratios evaluated, exceeding the upper limit of the equipment when the Mt solid/liquid ratio was higher than 1 g L^{-1} (data not shown).

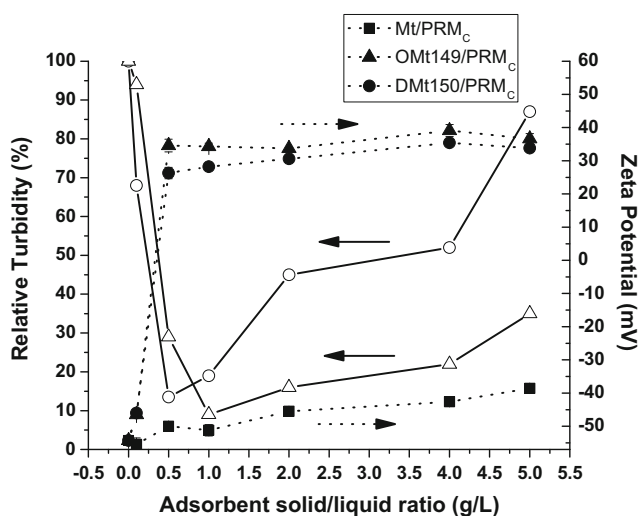


Fig. 7 Relative turbidity (empty symbols and solid line) and zeta potential (full symbols and dotted line) versus adsorbent concentration of indicated samples

A change in the ZP value of the initial suspension of PRMc from negative (-54.3 mV) to positive and constant (40 mV) was observed for organo-Mt/PRMc samples when solid/liquid ratios attained around 0.5 g L⁻¹. The sorption of PRM on these organo-Mt complexes did not change the ZP values (Table 1). Therefore, this behavior indicated the electrostatic interaction between the organo-Mt/PRMc surfaces (positively charged) and the negatively charged molecules of the adjuvants present in the PRMc producing the system flocculation. On the contrary, the repulsion between the adjuvant molecules and the negatively charged clay platelets of Mt prevented any flocculation and yielded an increment in the turbidity, as outlined previously.

Furthermore, when Mt/PRMc sample was used, a decrease in negative surface electric charge (without charge reversal, Fig. 7) was observed, reaching ZP values close to those of the Mt with the increase of the solid/liquid ratio.

Conclusions

The PRM adsorption behavior of a raw Mt from Patagonia, Argentina and three surfactant modified organo-Mt, with different loading amounts, was tested. The experimental PRM adsorption data indicated a PRM adsorption increase with the loading amount of each surfactant, assigned to hydrophobic interactions, except for BMT samples, due to the slight tendency of the PRM to adsorb on BTMA surfactant. The adsorption kinetics of PRM followed a PSO model, and the intraparticle diffusion process was also involved in the adsorption process. PRM desorption showed an irreversible behavior on Mt, which changed to reversible with the increase in surfactant loading.

XRD revealed a basal space shift of 0.14 nm with respect to the raw Mt sample, indicating the PRM entrance to the inter-layer space.

The characterization of the complexes formed after PRM sorption on organo-Mt showed that at low surfactant loading, the fungicide partly screened the negative charge of the clay surface; whereas at higher loading, the sorption occurred as neutral molecules through hydrophobic interactions with the organic cation as the surface ZP did not change. This mode of interaction was corroborated by FTIR spectroscopy.

To evaluate the potential application in technological systems for wastewater treatment, the samples that reached maximum PRM adsorption (DMt150 and OMt149) and Mt samples were used. The highest flocculation was attained for DMt150 and OMt149 samples with PRM adsorbed at solid/liquid ratios of around 0.5 and 1 g L⁻¹, respectively, where the electrostatic interaction between the organo-Mt/PRMc surfaces and PRMc adjuvant molecules reversed the ZP of the system from negative to positive. Therefore, the use of these organo-Mt samples (DMt150 and OMt149) may be promising

for the treatment of polluted waters with PRM, due to their large removal efficiency at a very low dose.

Acknowledgements Financial support of the Argentine Ministry of Science, Technology and Innovation—FONARSEC FS-Nano 008 and the Spanish Ministry of Economy and Competitiveness (Ref. CTM2013-42306-R, supported by funds from the European Regional Development Fund) and the Spanish Agency for International Cooperation for Development—Spanish Ministry of Education A/023433/10-09 is gratefully acknowledged. R.M.T.S. is a member of the National Council of Scientific and Technological Research (CONICET) and F.M. Flores acknowledges CONICET and Argentine (BEC.AR) fellowships.

References

- Akyuz S, Akyuz T (2003) FT-IR spectroscopic investigation of adsorption of pyrimidine on sepiolite and montmorillonite from Anatolia. *J Inclusion Phenom* 46:51–55
- Anfossi L, Sales P, Vanni A (2006) Degradation of anilinopyrimidine fungicides photoinduced by iron(III)-polycarboxylate complexes. *Pest Manag Sci* 62:872–879
- Araña J, Rodríguez CF, Melián JAH, Díaz OG, Peña JP (2008) Comparative study of photocatalytic degradation mechanisms of pyrimethanil, triadimenol, and resorcinol. *J Sol Energ-T Asme* 130:0410021–0410028
- Areco MM, dos Santos AM (2010) Copper, zinc, cadmium and lead bisorption by *Gymnogongrus torulosus*. Thermodynamics and kinetics studies. *Colloid Surface B* 81(2):620–628
- Baglieri A, Borzi D, Abbate C, Negro M, Gennari M (2009) Removal of fenhexamid and pyrimethanil from aqueous solutions by clays and organoclays. *J Environ Sci Health B* 44:220–225
- Bartelt-Hunt SL, Burns SE, Smith JA (2003) Nonionic organic solute sorption onto two organobentonites as a function of organic-carbon content. *J Colloid Interf Sci* 266:251–258
- Bianchi AE, Fernández M, Pantanetti M, Viña R, Torriani I, Torres Sánchez RM, Punte G (2013) ODTMA+ and HDTMA+ organo-montmorillonites characterization: new insight by WAXS, SAXS and surface charge. *Appl Clay Sci* 83-84:280–285
- Bulut E, Özacar M, Şengil IA (2008) Adsorption of malachite green onto bentonite: equilibrium and kinetic studies and process design. *Micropor Mesopor Mat* 115:234–246
- Cabras P, Angioni A (2000) Pesticide residues in grapes, wine, and their processing products. *J Agric Food Chem* 48:967–973
- Caiazza R, Kim YK, Xiao CL (2014) Occurrence and phenotypes of pyrimethanil resistance in *Penicillium expansum* from apple in Washington State. *Plant Dis* 98:924–928
- Crini G, Peindy HN, Gimbert F, Robert C (2007) Removal of C.I. Basic Green 4 (Malachite Green) from aqueous solutions by adsorption using cyclodextrin-based adsorbent: kinetic and equilibrium studies. *Sep Purif Technol* 53:97–110
- Cruz-Guzmán M, Celis R, Hermosín MC, Koskinen WC, Comejo J (2005) Adsorption of pesticides from water by functionalized organobentonites. *J Agr Food Chem* 53:7502–7511
- Dutta A, Singh N (2015) Surfactant-modified bentonite clays: preparation, characterization, and atrazine removal. *Environ Sci Pollut Res* 22:3876–3885
- EFSA (2006) Conclusion on the peer review of pyrimethanil. EFSA Scientific Report 61:1–70
- Flores FM, Gamba M, Torres Sánchez RM, Brendlé E, Brendlé J (2016) Microelectrophoresis and inverse gas chromatography as tools to study the surface interactions between a fluorinated fungicide and

- raw or organically modified Patagonian montmorillonite. *Appl Clay Sci* 134:83–88
- Foo KY, Hameed BH (2010) Insights into the modeling of adsorption isotherm systems. *Chem Eng J* 156:2–10
- Gamba M, Flores FM, Madejová J, Torres Sánchez RM (2015) Comparison of imazalil removal onto montmorillonite and nanomontmorillonite and adsorption surface sites involved: an approach for agricultural wastewater treatment. *Ind Eng Chem Res* 54:1529–1538
- Gamba M, Kovář P, Pospíšil M, Torres Sánchez RM (2017) Insight into thiabendazole interaction with montmorillonite and organically modified montmorillonites. *Appl Clay Sci* 137:59–68
- García-Antón J, Guiñón JL (1991) Determination of Hyamine 2389 critical micelle concentration (CMC) by means of conductometric, spectrophotometric and polarographic methods. *Colloid Surface A* 61:137–145
- Ghimici L, Nichifor M (2012) Flocculation by cationic amphiphilic polyelectrolyte: relating efficiency with the association of polyelectrolyte in the initial solution. *Colloid Surface A* 415:142–147
- Gil FN, Moreira-Santos M, Chelinho S, Pereira C, Feliciano JR, Leitão JH, Sousa JP, Ribeiro R, Viegas CA (2015) Suitability of a *Saccharomyces cerevisiae*-based assay to assess the toxicity of pyrimethanil sprayed soils via surface runoff: comparison with standard aquatic and soil toxicity assays. *Sci Total Environ* 505:161–171
- Gu Z, Gao M, Lu L, Liu Y, Yang S (2015) Montmorillonite functionalized with zwitterionic surfactant as a highly efficient adsorbent for herbicides. *Ind Eng Chem Res* 54:4947–4955
- Guégan R, Giovanela M, Warmont F, Motelica-Heino M (2015) Nonionic organoclay: a ‘Swiss Army knife’ for the adsorption of organic micro-pollutants? *J Colloid Interf Sci* 437:71–79
- He H, Ma Y, Zhu J, Yuan P, Qing Y (2010) Organoclays prepared from montmorillonites with different cation exchange capacity and surfactant configuration. *Appl Clay Sci* 48:67–72
- Hojiyev R, Ersever G, Karaağaçlıoğlu IE, Karakaş F, Boylu F (2016) Changes on montmorillonite characteristics through modification. *Appl Clay Sci* 127–128:105–110
- Hu B, Luo H, Chen H, Dong T (2011) Adsorption of chromate and par-nitrochlorobenzene on inorganic-organic montmorillonite. *Appl Clay Sci* 51:198–201
- Kilisioglu A, Bilgin B (2003) Thermodynamic and kinetic investigations of uranium adsorption on amberlite IR-118H resin. *Appl Radiat Isotopes* 58:155–160
- Komárek M, Čadková E, Chrástný V, Bordas F, Bollinger JC (2010) Contamination of vineyard soils with fungicides: a review of environmental and toxicological aspects. *Environ Int* 36:138–151
- Kuo C-Y, Wu C-H, Wu J-Y (2008) Adsorption of direct dyes from aqueous solutions by carbon nanotubes: determination of equilibrium, kinetics and thermodynamics parameters. *J Colloid Interf Sci* 327:308–315
- Latorre BA, Spadaro I, Rioja ME (2002) Occurrence of resistant strains of *Botrytis cinerea* to anilinopyrimidine fungicides in table grapes in Chile. *Crop Prot* 21:957–961
- Lombardi B, Baschini M, Torres Sánchez RM (2003) Optimization of parameters and adsorption mechanism of thiabendazole fungicide by a montmorillonite of North Patagonia, Argentina. *Appl Clay Sci* 24:43–50
- Magnoli AP, Tallone L, Rosa CAR, Dalcero AM, Chiacchiera SM, Torres Sanchez RM (2008) Commercial bentonites as detoxifier of broiler feed contaminated with aflatoxin. *Appl Clay Sci* 40:63–71
- Majdan M, Bujacka M, Sabah E, Gładysz-Płaska A, Pikus S, Sternik D, Komosa Z, Padewski A (2009) Unexpected difference in phenol sorption on PTMA- and BTMA-bentonite. *J Environ Manag* 91:195–205
- Maqueda C, Dos Santos AM, Morillo E, Torres Sánchez RM, Perez-Sayago M, Undabeytia T (2013) Adsorption of diuron on mechanically and thermally treated montmorillonite and sepiolite. *Appl Clay Sci* 72:175–183
- Marco-Brown JL, Areco MM, Torres Sánchez RM, Dos Santos AM (2014) Adsorption of picloram herbicide on montmorillonite: kinetic and equilibrium studies. *Colloid Surface A* 449:121–128
- Mo J, Dai L, Chen L, Wang Y, Huang A, Wang L, Ma L (2015) Structural effects of organobentonites on controlled release of pretilachlor. *Appl Clay Sci* 115:150–156
- Morillo E, Undabeytia T, Cabrera A, Villaverde J, Maqueda C (2004) Effect of soil type on adsorption-desorption, mobility, and activity of the herbicide norflurazon. *J Agr Food Chem* 52:884–890
- Nir S, Undabeytia T, Yaron-Marcovich D, El-Nahhal Y, Polubesova T, Serban C, Rytwo G, Lagaly G, Rubin B (2000) Optimization of adsorption of hydrophobic herbicides on montmorillonite preadsorbed by monovalent organic cations: interaction between phenyl rings. *Environ Sci Technol* 34:1269–1274
- Özcan AS, Erdem B, Özcan A (2005) Adsorption of Acid Blue 193 from aqueous solutions onto BTMA-bentonite. *Colloid Surface A* 266:73–81
- Para G, Hamerska-Dudra A, Wilk KA, Warszyński P (2011) Mechanism of cationic surfactant adsorption—effect of molecular structure and multiple charge. *Colloid Surface A* 383:67–72
- Patel HA, Somani RS, Bajaj HC, Jasra RV (2010) Synthesis of organoclays with controlled particle size and whiteness from chemically treated Indian bentonite. *Ind Eng Chem Res* 49:1677–1683
- Pecini EM, Avena MJ (2013) Measuring the isoelectric point of the edges of clay mineral particles: the case of montmorillonite. *Langmuir* 29:14926–14934
- Polubesova T, Rytwo G, Nir S, Serban C, Margulies L (1997) Adsorption of benzyltrimethylammonium and benzyltriethylammonium on montmorillonite: experimental studies and model calculations. *Clay Clay Miner* 45:834–841
- PPDB: Pesticide Properties DataBase (2011) University of Hertfordshire: Hatfield, Hertfordshire. <http://sitem.herts.ac.uk/aeru/iupac/Reports/573.htm>
- Ren W, Teng Y, Zhou Q, Paschke A, Schüürmann G (2014) Sorption of chlorimuron-ethyl on montmorillonite clays: effects of exchangeable cations, pH, and ionic strength. *Environ Sci Pollut Res* 21:11587–11597
- Rosen MJ (1989) Surfactants and interfacial phenomena. York, New
- Rytwo G, Lavi R, Rytwo Y, Monchase H, Dultz S, König TM (2013) Clarification of olive mill and winery wastewater by means of clay-polymer nanocomposites. *Sci Total Environ* 442:134–142
- Sagitova EA, Donfack P, Prokhorov KA, Nikolaeva GY, Gerasin VA, Merekalova ND, Materny A, Antipov EM, Pashinin PP (2009) Raman spectroscopic characterization of the interlayer structure of Na⁺-montmorillonite clay modified by dodecyl dimethyl ammonium bromide. *J Phys Chem B* 113:7482–7490
- Savic IM, Stojiljkovic S, Savic I, Gajic D (2014) Industrial application of clays and clay minerals. In: Wesley LR clays and clay minerals: geological origin, mechanical properties and industrial applications, 1st edn. Nova Science Publishers, Inc, pp 379–402
- Seeland A, Oehlmann J, Müller R (2012) Aquatic ecotoxicity of the fungicide pyrimethanil: effect profile under optimal and thermal stress conditions. *Environ Pollut* 168:161–169
- Sholberg PL, Bedford K, Stokes S (2005) Sensitivity of *Penicillium* spp. and *Botrytis cinerea* to pyrimethanil and its control of blue and gray mold of stored apples. *Crop Prot* 24:127–134
- Singh N, Tandon S (2015) Dissipation kinetics and leaching of cyazofamid fungicide in texturally different agricultural soils. *Int J Environ Sci Te* 12(8):2475–2484
- Smith JA, Galan A (1995) Sorption of nonionic organic contaminants to single and dual organic cation bentonites from water. *Environ Sci Technol* 29:685–692
- Stofela SKF, de Almeida Neto AF, Gimenes ML, Vieira MGA (2015) Adsorption of toluene into commercial organoclay in liquid phase:

- kinetics, equilibrium and thermodynamics. *Can J Chem Eng.* doi: [10.1002/cjce.22174](https://doi.org/10.1002/cjce.22174). Accepted 18 Jul 2014
- Sun Z, Park Y, Zheng S, Ayoko GA, Frost RL (2013) XRD, TEM, and thermal analysis of Arizona Ca-montmorillonites modified with didodecyldimethylammonium bromide. *J Colloid Interf Sci* 408: 75–81
- Teh CY, Budiman PM, Shak KPY, Wu TY (2016) Recent advancement of coagulation-flocculation and its application in wastewater treatment. *Ind Eng Chem Res* 55(16):4363–4389
- Tong DS, Zhou CH, Lu Y, Yu H, Zhang GF, Yu WH (2010) Adsorption of Acid Red G dye on octadecyl trimethylammonium montmorillonite. *Appl Clay Sci* 50:427–431
- Undabeytia T, Recio E, Maqueda C, Sánchez-Verdejo T, Balek V (2012) Slow diuron release formulations based on clay-phosphatidylcholine complexes. *Appl Clay Sci* 55:53–61
- Ünlü N, Ersoz M (2006) Adsorption characteristics of heavy metal ions onto a low cost biopolymeric sorbent from aqueous solutions. *J Hazard Mater B* 136:272–280
- Vanni A, Fontana F, Gignetti A, Gennari M (2003) Behaviour of pyrimethanil in soil: abiotic and biotic processes. In *Proceedings of the XII Symposium of Pesticide Chemistry, Piacenza, Italy*, pp 233–238
- Vanni A, Anfossi L, Cignetti A, Baglieri A, Gennari M (2006) Degradation of pyrimethanil in soil: influence of light, oxygen, and microbial activity. *J Environ Sci Health B* 41:67–80
- Verdisson S, Couderchet M, Vernet G (2001) Effects of procymidone, fludioxonil and pyrimethanil on two non-target aquatic plants. *Chemosphere* 44:467–474
- Wong TC, Wong NB, Tanner PA (1997) A fourier transform IR study of the phase transitions and molecular order in the hexadecyltrimethylammonium sulfate/water system. *J Colloid Interf Sci* 186:325–331
- Xi Y, Ding Z, He H, Frost RL (2004) Structure of organoclays—an X-ray diffraction and thermogravimetric analysis study. *J Colloid Interf Sci* 277:116–120